# CHARACTERISTICS OF KINEMATICS OF A CORONAL MASS EJECTION DURING THE 2010 AUGUST 1 CME–CME INTERACTION EVENT

Manuela Temmer[1], Bojan Vršnak[2], Tanja Rollett[1], Bianca Bein[1], Curt A. de Koning[3], Ying Liu[4,5], Eckhard Bosman[6], Jackie A. Davies[7], Christian Möstl[1,4,6], Tomislav Žic[2], Astrid M. Veronig[1], Volker Bothmer[7], Richard Harrison[8], Nariaki Nitta[9], Mario Bisi[10,11], Olga Flor[1], Jonathan Eastwood[12], Dusan Odstrcil[13], and Robert Forsyth[12]

[1] Kanzelhöhe Observatory-IGAM, Institute of Physics, University of Graz, Universitätsplatz 5, A-8010 Graz, Austria; mat@igam.uni-graz.at
[2] Hvar Observatory, Faculty of Geodesy, University of Zagreb, Kačićeva 26, HR-10000 Zagreb, Croatia
[3] NOAA Space Weather Prediction Center, Boulder, CO 80305, USA
[4] Space Sciences Laboratory, University of California, Berkeley, CA 94720, USA
[5] State Key Laboratory of Space Weather, National Space Science Center, Chinese Academy of Sciences, Beijing, China
[6] Space Research Institute, Austrian Academy of Sciences, A-8042 Graz, Austria
[7] Institut für Astrophysik, Göttingen University, Friedrich-Hund Platz 1, D-37077 Göttingen, Germany
[8] RAL Space, Rutherford Appleton Laboratory, Harwell Oxford, Didcot OX11 0QX, UK
[9] Solar and Astrophysics Laboratory, Lockheed Martin Advanced Technology Centre, Palo Alto, CA 94304-1191, USA
[10] Institute of Mathematics and Physics, Aberystwyth University, Ceredigion SY23 3BZ, UK
[11] Center for Astrophysics and Space Sciences, University of California, San Diego, La Jolla, CA 92093-0424, USA
[12] The Blackett Laboratory, Imperial College London, London SW7 2AZ, UK
[13] Computational and Data Sciences, George Mason University/NASA Goddard Space Flight Center, Mail Code 674, Greenbelt, MD 20771, USA

## ABSTRACT

We study the interaction of two successive coronal mass ejections (CMEs) during the 2010 August 1 events using *STEREO*/SECCHI COR and heliospheric imager (HI) data. We obtain the direction of motion for both CMEs by applying several independent reconstruction methods and find that the CMEs head in similar directions. This provides evidence that a full interaction takes place between the two CMEs that can be observed in the HI1 field of view. The full de-projected kinematics of the faster CME from Sun to Earth is derived by combining remote observations with in situ measurements of the CME at 1 AU. The speed profile of the faster CME (CME2; ∼1200 km s$^{-1}$) shows a strong deceleration over the distance range at which it reaches the slower, preceding CME (CME1; ∼700 km s$^{-1}$). By applying a drag-based model we are able to reproduce the kinematical profile of CME2, suggesting that CME1 represents a magnetohydrodynamic obstacle for CME2 and that, after the interaction, the merged entity propagates as a single structure in an ambient flow of speed and density typical for quiet solar wind conditions. Observational facts show that magnetic forces may contribute to the enhanced deceleration of CME2. We speculate that the increase in magnetic tension and pressure, when CME2 bends and compresses the magnetic field lines of CME1, increases the efficiency of drag.

*Key words:* Sun: corona – Sun: coronal mass ejections (CMEs)

*Online-only material:* animation, color figures

## 1. INTRODUCTION

On 2010 August 1 a total of five coronal mass ejections (CMEs) could be identified. All CMEs were launched from source regions (SRs) located on the Earth-directed hemisphere of the Sun, which made them potential geoeffective space weather events (for an overview of all these CME events see Harrison et al. 2012). Schrijver & Title (2011) presented a detailed study focusing on the 2010 August 1 CME-associated solar surface activity using observations from the *Solar Terrestrial Relations Observatory* (*STEREO*) and the *Solar Dynamics Observatory*. They showed how complex and widely distributed the magnetic field line connections were over the solar surface that finally caused the initiation and evolution of the observed eruptions. In fact, the eruptions affected half of the solar corona, which makes it necessary to analyze many aspects of these events in detail.

Two of the CME events on 2010 August 1 (named as M- and L-tracks in the overview paper by Harrison et al. 2012) were launched in quick succession from SRs located close together (Harrison et al. 2012). Furthermore, as we shall show, the first event was slower than the second event; hence, the CMEs are expected to interact with each other at a certain distance from

the Sun. It has been suggested by Gopalswamy et al. (2001) and Burlaga et al. (2002) that during the interaction process the CMEs may merge and become a single magnetic structure. Using observations from *STEREO* for the 2007 January 24–25 events, Lugaz et al. (2008) and Webb et al. (2009) reported the overtaking of a slower CME by a faster CME such that the shock wave driven by the faster CME traveled through the slower preceding CME (Lugaz et al. 2009). The studies by Lugaz et al. (2008, 2009) and Webb et al. (2009) revealed that knowing the propagation direction of the potentially interacting CMEs is crucial in order to interpret the observations in a reliable way. Furthermore, enhanced radio emission (Gopalswamy et al. 2001) and highly energetic solar particles have been reported in connection with a CME–CME interaction (e.g., Kahler 1994, 2001; Gopalswamy et al. 2002). Numerical simulations have shown that this is either due to the reconnection processes between the intrinsic magnetic fields of the CMEs, or the additional particle acceleration due to the associated shock wave propagating through the slower CME (e.g., Schmidt & Cargill 2004; Lugaz et al. 2005). All these results provide evidence that the intrinsic magnetic field of a CME, i.e., the assumed flux-rope structure (e.g., Chen 1996; Low 2001, and references therein), plays an important role with respect to its kinematical evolution.

**Table 1**
Direction (dir) and Speed ($v$) of CME1 and CME2 Derived from SECCHI Observations by Applying Different Methods for Different FoVs

| Method | $\text{dir}_{CME1}$ | | $\text{dir}_{CME2}$ | | $v_{CME1}$ | $v_{CME2}$ | FOV |
|---|---|---|---|---|---|---|---|
| SR | E14 | N14 | E35 | N20 | ... | ... | EUVI |
| R+IS | ... | ... | E13 ± 10 | ... | ... | 720 ± 80 | HI1+HI2+*Wind* |
| forw | E20 ± 10 | N9 ± 5 | E28 ± 5 | N20 ± 5 | 650 ± 150 | 1160 ± 200 | COR1+2 |
| mass | E5 ± 5 | ... | E6 ± 5 | ... | 740 ± 140 | 1250 ± 100 | COR1+2 |
| polar | E19 ± 8 | N1 ± 2 | E41 ± 5 | N22 ± 2 | 616 ± 26 | 1264 ± 66 | COR1+2 |
| triang | E21 ± 9 | ... | E20 ± 5 | ... | 732 ± 350 | 1138 ± 550 | COR2+HI1 (A+B) |
| FP/HM | ... | ... | E2/E36 | ... | ... | 764/960 | HI1+HI2 |

**Notes.** The source region (SR) location is determined from low-coronal signatures of each CME as observed in EUVI data (see Figures 1 and 2). We present results from combined remote sensing and in situ data (R+IS) from *STEREO-A* and *Wind*, respectively, the forward modeling (forw), calculating the "true" mass from stereoscopic *STEREO-A* and *STEREO-B* images (mass), the polarimetric localization technique (polar), geometric triangulation (triang), and harmonic mean and fixed phi fitting method (FP/HM). For a description of each method see Section 3.1.

As a CME propagates into interplanetary (IP) space it interacts with the ambient medium and transfers momentum and energy in the form of magnetohydrodynamic (MHD) waves (e.g., Jacques 1977). The interaction of the CME with the solar wind results in the adjustment between the speed of the CME and the solar wind flow. Assuming that the main force that governs the propagation behavior of a CME in IP space is the "aerodynamic" drag force (Cargill et al. 1996; Vršnak 2001; Vršnak & Gopalswamy 2002; Cargill 2004), we may attempt to simulate the kinematical profile of a CME by using the drag-based model (DBM) proposed by Vršnak & Žic (2007), and advanced by Vršnak et al. (2012).

In the following study we focus on two CME events from 2010 August 1 and we investigate if the CMEs may have interacted with each other as they propagated away from the Sun. We use *STEREO*/SECCHI observations to derive the three-dimensional properties of both CMEs (direction of motion, kinematical profile, width). The derived de-projected kinematical profile is then compared to the results from the DBM. From this we will show that (1) both CMEs head in similar directions as they evolve into IP space, making a CME–CME interaction highly likely; (2) a strong deceleration of the faster CME can be explained by interaction with the slower CME, which can be represented as an ambient medium of higher density and flow speed compared to the unperturbed solar wind; and (3) the interaction between the magnetic structures of the CMEs starts earlier than their leading edges merging in the heliospheric images.

## 2. DATA AND OBSERVATIONS

For the CME–CME interaction study we analyze white-light images from the *STEREO* (*STEREO-A* and *STEREO-B*) SECCHI instrument suite (Howard et al. 2008). SECCHI consists of two coronagraphs, COR1 and COR2, covering a plane-of-sky (POS) distance range up to $\sim$15 $R_\odot$, and the heliospheric imagers (HIs), HI1 and HI2, for distances > 15 $R_\odot$. This instrument combination allows us to track CME/ICME events in the inner heliosphere from $\sim$2 $R_\odot$ to beyond 1 AU. For context information on the low-coronal conditions close to the solar surface, we use data from the SECCHI Extreme Ultraviolet Imager (EUVI; Wuelser et al. 2004).

Due to an observational gap, *STEREO-B* data are not available from $\sim$10:00 UT on 2010 August 1 until 04:00 UT on 2010 August 2. For that reason, techniques based on stereoscopic data are used close to the Sun but not for studying the entire propagation path up to 1 AU.

The first CME (hereinafter CME1) was launched from the Sun on 2010 August 1 at $\sim$2:55 UT with a de-projected mean speed of $\sim$700 km s$^{-1}$ in the COR1 and COR2 fields of view (FOVs). *STEREO-A* EUVI images (Figure 1, top right) show an off-limb dimming region, representing the low-coronal signatures of CME1. From the solar surface signatures we also derive the location of SR for both CMEs as given in Table 1 (cf. Cremades & Bothmer 2004). As can be seen from Figure 2, the CME feature can be seamlessly tracked as it propagates into the coronagraph FoV from which it can be further followed into the HI1 FoV. The CME was associated with a prominence eruption followed by a *GOES* B4.5 class flare in a small active region (NOAA 11094; cf. Schrijver & Title 2011) located at E14/N14 (if not stated otherwise all locations are heliographic coordinates given in degrees with respect to Earth).

The second CME (hereinafter CME2) was associated with a long-duration flare classified as *GOES* C3.8 and was launched from AR 11092 located at about E35/N20. The flare started at $\sim$7:24 UT, lasted until 10:25 UT and had its maximum intensity at 08:56 UT (for more details on the flare and associated filament eruption see Liu et al. 2010a; Schrijver & Title 2011). CME2 was a fast event with a de-projected mean speed of $\sim$1200 km s$^{-1}$ in the COR1 and COR2 FoVs. Clear low-coronal signatures of CME2 are seen in *STEREO-A* EUVI at $\sim$7:45 UT (see bottom right panel of Figure 1). CME2 can be seamlessly tracked from EUVI to COR1 (Figure 2) where it shows a very distinct leading edge and is associated with a remote streamer deflection, probably related to a shock front (cf. Liu et al. 2009; Gopalswamy et al. 2009; Ontiveros & Vourlidas 2009).

The in situ signature of the leading edge of CME2 was an IP shock and its high-density sheath region recorded at 1 AU on 2010 August 3 17:05 UT (cf. Harrison et al. 2012) by *Wind*/SWE/MFI (Ogilvie et al. 1995; Lepping et al. 1995). The arrival time of the shock and proton bulk speed following its arrival are used to further constrain the kinematical profile of CME2 (see Section 3.1.4). The solar wind speed diagnosed in situ near Earth was around 400 km s$^{-1}$ prior to the arrival of the shock associated with CME2 on 2010 August 3. The solar wind speed measured in the sheath region of CME2 increased to 600 km s$^{-1}$ (see Figure 14 in Harrison et al. 2012). A detailed study focusing on the in situ signatures of these events is given by Möstl et al. (2012). The readers are also directed to Liu et al. (2012) for connections between imaging observations and in situ signatures with respect to the CME–CME interaction.

CME2 was associated with a type II radio burst showing distinct morphological changes at $\sim$09:50 UT on 2010 August 1. Emission at the fundamental frequency divided into
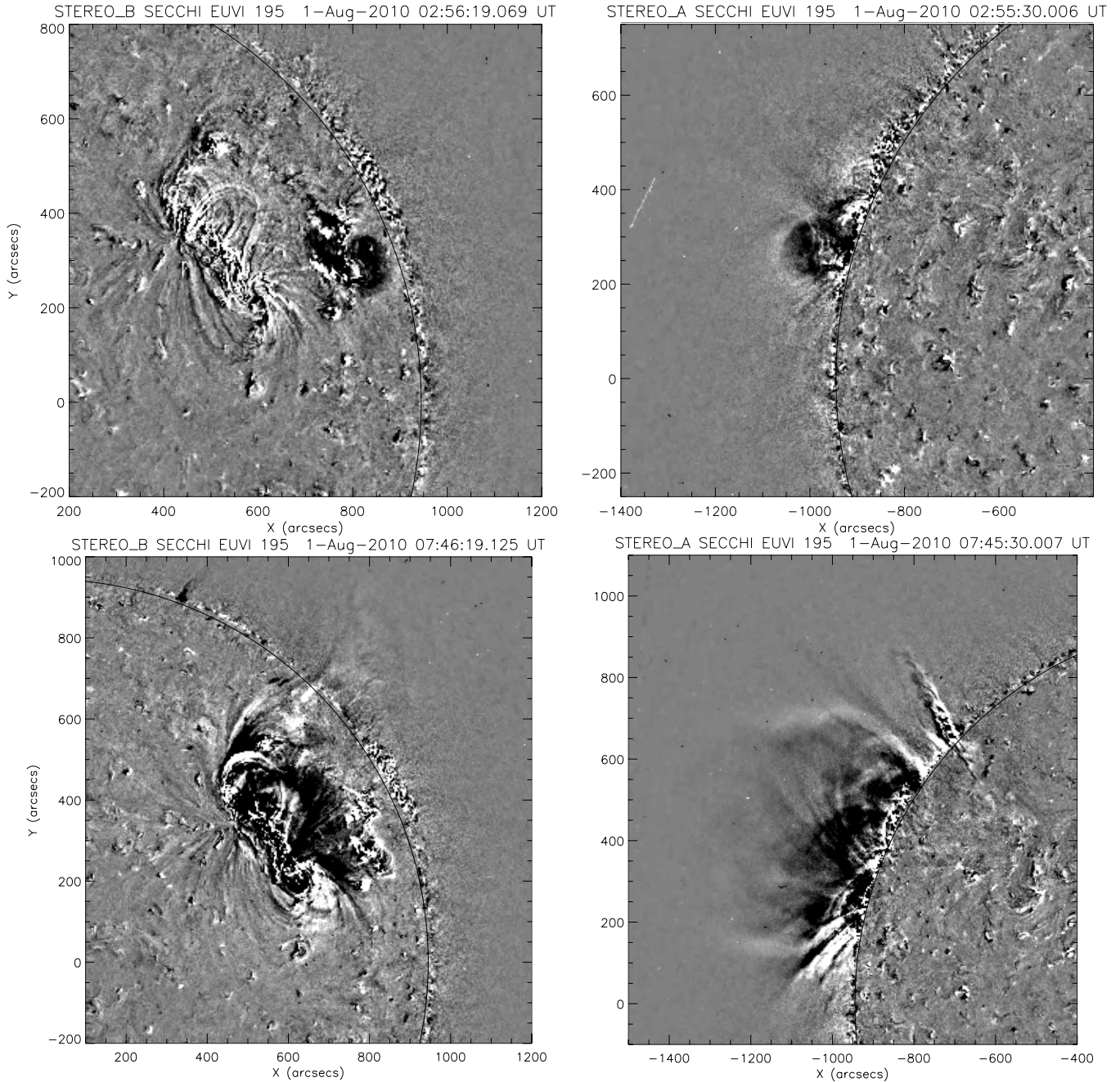
**Figure 1.** *STEREO-A* (right) and *-B* (left) EUVI 195 Å difference images showing the coronal dimming regions of CME1 (top) and CME2 (bottom).

two branches of different frequency drifts, implying the simultaneous existence of radio emission sites moving with different speeds. More details on the radio signatures associated with the 2010 August 1 events are given by Martinez Oliveros et al. (2012).

## 3. METHODS

### 3.1. Observations and Reconstruction Methods

In the following section, we give details on different reconstruction methods used to obtain the three-dimensional characteristics of CME1 and CME2. Most important, we derive the direction of motion for both CMEs in order to give evidence of an actual interaction. For more details on different reconstruction techniques for stereoscopic data of CMEs in the early phase

of the *STEREO* mission we refer the interested reader to Mierla et al. (2010).

#### 3.1.1. Forward Modeling

The flux-rope forward fitting model developed by Thernisien et al. (2006, 2009) is a raytrace simulation method that computes synthetic total and polarized brightness images using the Thomson scattering formulae from an assumed electron density model. The appearance of a CME is approximated by a flux-rope-like structure which is simulated by the graduated cylindrical shell model. By fitting the density model to contemporaneous image pairs from *STEREO-A* and *STEREO-B*, which observe the CME from two different vantage points, we derive characteristic CME parameters like width and SR position, i.e.,
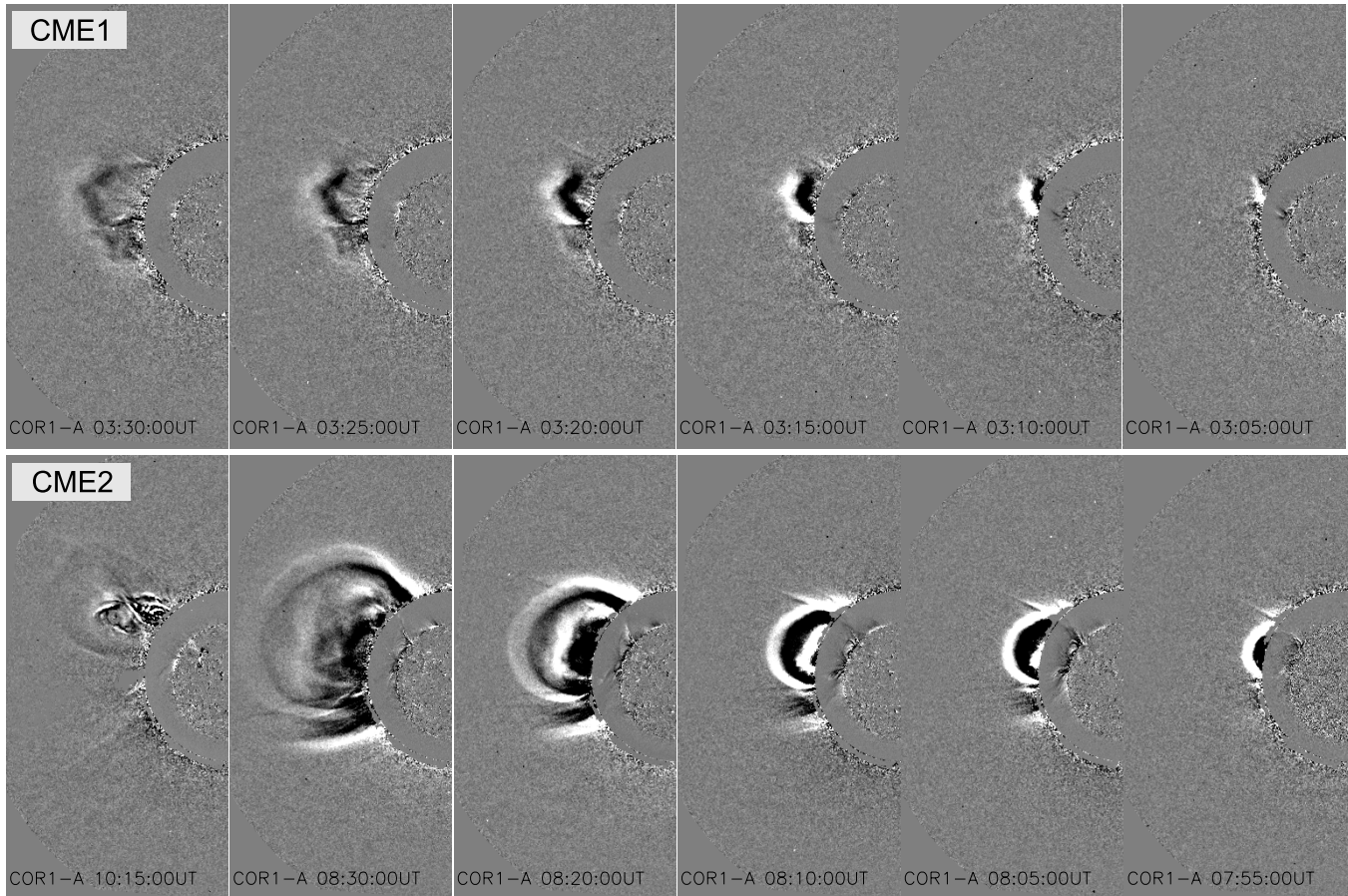
**Figure 2.** CME1 and CME2 in EUV and white-light observations. Top: sequence of EUVI/COR1 *STEREO-A* running difference images of CME1. Bottom: sequence of EUVI/COR1 *STEREO-A* running difference images of CME2.

the location of the CME apex projected back along a straight line normal to the solar surface (Thernisien 2011). For the reconstruction we chose those image pairs with the highest contrast and applied the forward modeling to imagery data from COR1 for CME1 and COR2 for CME2.

### 3.1.2. Geometric Triangulation

The geometric triangulation technique developed by Liu et al. (2010b, 2010c) can convert elongation measurements to radial distance and propagation direction, taking advantage of stereoscopic imaging observations from *STEREO-A* and *STEREO-B*. The basis of this technique is that the propagation direction and distance yield a certain elongation angle corresponding to the viewpoint. The two viewpoints from *STEREO* then form a simple geometry with which the propagation direction and radial distance can be derived. The advantage of this technique is that it has no free parameters and does not assume a constant propagation direction and speed. This is of particular importance in the case of CME–CME interactions, as both the propagation direction and speed can be changed by the interactions. Liu et al. (2010b, 2010c) describe the mathematical formulae and detailed procedures for applying this technique. Here we apply the technique to CME1 and CME2 before their tentative collision. Because of a data gap in *STEREO-B*, the technique can be applied to COR2 and HI1 for CME1 and only to COR2 for CME2 (cf. Figure 5 in Harrison et al. 2012).

### 3.1.3. Fitting Method for Harmonic Mean and Fixed Phi

We also make use of two well-established fitting techniques, namely, the so-called fixed phi (FP) fitting method developed by Sheeley and coworkers (Sheeley et al. 1999, 2008; Kahler & Webb 2007; Rouillard et al. 2008) and the harmonic mean (HM) fitting method developed by Lugaz (2010) to find constant propagation directions and speeds. The former technique effectively assumes that we are tracing a point-like source along a particular radial line from the Sun, the latter assumes a circular geometry for the CME. The fitting techniques are applied to elongation–time profiles derived from single spacecraft observations from both HI1 and HI2 for CME1 and CME2 under the assumption that the CME is moving with constant speed and in a constant direction. For a detailed application of this method to the data of 2010 August 1 we refer to Harrison et al. (2012).

### 3.1.4. Remote Sensing and In Situ Data

By combining observations from remote sensing instruments on a single spacecraft and in situ observations of CME signatures at 1 AU, we are able to estimate the direction of motion of a CME as well as its de-projected kinematics (Möstl et al. 2009, 2010; Rollett et al. 2012). The time–elongation profile of CME2 for the distance range from $\sim$15 $R_\odot$ to Earth is obtained from an elongation–time map made from *STEREO-A* HI1 and HI2 observations extracted along the ecliptic plane (so-called J-maps; Sheeley et al. 2008; Davies et al. 2009). We convert the elongations into radial distances by assuming a constant

direction of motion from Sun to Earth (Möstl et al. 2009) and applying the HM conversion method, i.e., assuming a circular geometry for the CME (e.g., Howard & Tappin 2009; Lugaz et al. 2009). The measured arrival time and speed of the shock and its following high-density sheath region at 1 AU are boundary conditions for the conversion method and constrain the possible range for the direction of motion of the CME under study. From this we obtain two directions, one that matches the arrival time and one that matches the arrival speed (for more details on the method see Rollett et al. 2012). We note that the average of these two directions is taken as final result. Another boundary condition close to the Sun is represented by the kinematical profile of CME2 as derived from COR2 observations which slightly overlap the FoV of HI1. By combining distance–time and speed–time profiles up to ∼15 $R_\odot$ and at 1 AU with results from the conversion method which covers the distance range that lies in between, we derive the full kinematical profile of CME2 from Sun to Earth (see also Temmer et al. 2011).

This method is applied solely to CME2 since the signature of CME1 cannot be tracked to the distance of 1 AU in remote sensing images. Furthermore, only the shock driven by CME2 could be clearly identified at 1 AU from in situ *Wind* data. Liu et al. (2012) suggest that both CME1 and CME2 were observed in situ; however, this cannot be completely confirmed from the data.

### 3.1.5. Total Mass

CMEs observed from different vantage points appear differently in their intensity distribution and thus apparent morphology, which is basically due to the line-of-sight integration of the white-light emission from optically thin structures. The differences in the total intensity are due to the different incident angles of the Thomson scattering geometry through the CME plasma (see Colaninno & Vourlidas 2009). Combining observations from both *STEREO* spacecraft enables us to estimate the direction of motion of the CME as well as its total ("true") mass (Colaninno & Vourlidas 2009). The total mass is calculated for CME1 as well as CME2 by using stereoscopic image pairs from COR1 and COR2.

### 3.1.6. Polarimetric Localization

Applying the polarimetric localization technique (de Koning & Pizzo 2011), the percent polarization observed by a single coronagraph is used to obtain a three-dimensional reconstruction of a whole CME. Polarimetric localization is based on the equations of Billings (1966), in which the elongation angle of a scattering point and the measured percent polarization can be related to the distance that the scattering point is from the POS. Two possible solutions are derived from this method, one ahead of the spacecraft POS, and one behind the POS. The polarimetric localization solution from *STEREO-A* which is collocated with the one from *STEREO-B* gives the correct solution. From the whole CME reconstruction, the direction of motion as well as the kinematics of the CME in three-dimensional space is estimated. This method is applied independently to COR1 and COR2 images from *STEREO-A* and *STEREO-B* for both CME1 and CME2.

### 3.2. Simulation of Kinematics of CME2 Using the DBM

The DBM (Vršnak et al. 2012) is based on the assumption that the kinematical profile of a CME in IP space is mainly controlled by drag force (Cargill et al. 1996; Vršnak 2001; Vršnak &

Gopalswamy 2002; Cargill 2004; Vršnak & Žic 2007). The drag force can be expressed in its simplest form as

$$F_D = \gamma(v - w)|v - w|,$$

with $w$ the solar wind speed and $v$ the CME speed. The drag parameter $\gamma$ is defined as

$$\gamma = C_d \frac{A_{\mathrm{CME}} \rho_{\mathrm{sw}}}{m_{\mathrm{CME}}},$$

where $C_d$ is the drag coefficient, $A_{\mathrm{CME}}$ is the cross-sectional area of the CME, $\rho_{\mathrm{sw}}$ is the density of the solar wind, and $m_{\mathrm{CME}}$ is the mass of the CME (cf. Cargill 2004). $C_d$ is a dimensionless number, typically of order of unity (see Batchelor 1967). Working on this assumption, we calculate the kinematical profile of CME2 and compare it with the kinematical profile derived from observations.

As input parameters, DBM requires the launch time $t_0$ and speed of the CME $v_0$ at a certain distance from the Sun $R_0$, the asymptotic solar wind speed $w$ at 1 AU as well as $\gamma$. From white-light observations, we derive $t_0$, $v_0$, and $R_0$, while $w$ is taken directly from *Wind* data. For $\gamma$ we obtain the parameters $A_{\mathrm{CME}}$ and $m_{\mathrm{CME}}$ from stereoscopic reconstruction methods, and $\rho_{\mathrm{sw}}$ is calculated using the empirical formula developed by Leblanc et al. (1998) depending only on the radial distance from the Sun. Assuming that a CME expands in a self-similar manner and that the density falls off as distance squared, $\gamma$ can be kept constant for the distance range from Sun to Earth. For a detailed description of the DBM we refer to Vršnak et al. (2012). The DBM is available for public usage through a Web interface under http://oh.geof.unizg.hr/CADBM/cadbm.php.

## 4. RESULTS

Figure 3 shows base difference images and J-maps for HI1-A data from which we observe that the signatures of the leading edge of CME1 and CME2 merged somewhere between 14:00 and 16:00 UT, corresponding to a distance of ∼38 ± 5 $R_\odot$. After the interaction, no identifiable signatures of CME1 were observed, i.e., CME1 was "lost" in the white-light signature of CME2.

Figure 4 shows the simulated flux-rope model (see Section 3.1.1) overlaid on white-light COR1 (for CME1) and COR2 (for CME2) images. Applying this model, we derive the radial back-projection of the CME apex onto the solar surface, which represents the launch site of the CME (CME1: E20/N09; CME2: E28/N20), the tilt angle relative to the solar equator (CME1: 39°; CME2: 47°), the face-on width (CME1: ∼68°; CME2: ∼100°), and the edge-on width (CME1: ∼23°; CME2: ∼52°). Typical uncertainties lie in the range of ±10° and depend on the identified boundaries of the CME.

The top panel of Figure 5 shows how the Billings (1966) equations are used to obtain a reconstructed point within a CME relative to the spacecraft POS (see Section 3.1.6). The bottom panels show two possible reconstructed CMEs for each event based on *STEREO-A* percent polarization measurements, one ahead of the spacecraft POS, and one behind the POS. The correct reconstruction, which can be deduced by utilizing in addition *STEREO-B* percent polarization measurements, is the colored reddish-orange one traveling eastward of the Sun–Earth line (i.e., ahead of the spacecraft POS). What can be seen immediately is that both CMEs have a similar trajectory, and that CME2 is significantly larger than CME1.
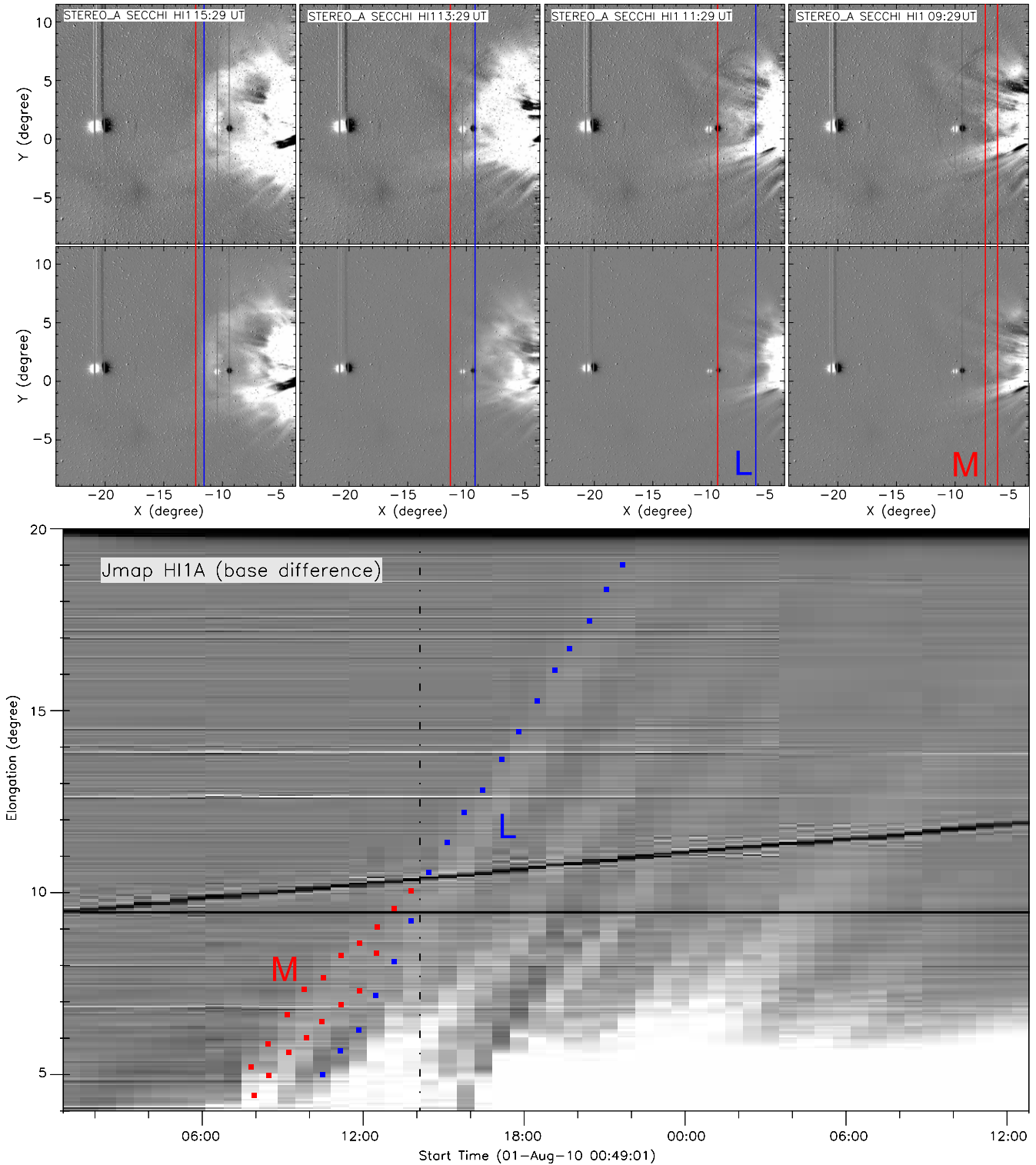
**Figure 3.** Top: base difference images from HI1-A showing the evolution of CME1 and CME2 for the distance range ∼20–40 $R_\odot$. The frontal parts of CME1 (M) and CME2 (L) are indicated by red and blue vertical lines, respectively. Different contrast is used for top and bottom panels in order to better visualize CME1, which is fainter (less massive) than CME2. See also the accompanying movie. Bottom: J-map constructed from base difference images and overplotted tracks of CME1 (M; red squares) and CME2 (L; blue squares).

(An animation and a color version of this figure are available in the online journal.)

Table 1 gives a summary of results for the direction of motion and speed of CME1 and CME2, respectively, derived from using the different methods described in Section 3.1. We find that both ejecta propagate in similar directions which makes an interaction between both CMEs within the FoV of HI1-A highly likely.

Due to the unknown geometry of the CMEs we are not able to determine which method delivers the most reliable result. Taking the average of all methods used, we derive for CME1 the direction E16° ± 7° which is close to its SR located at E14 (cf. Figure 1). For CME2 we derive the average longitude of
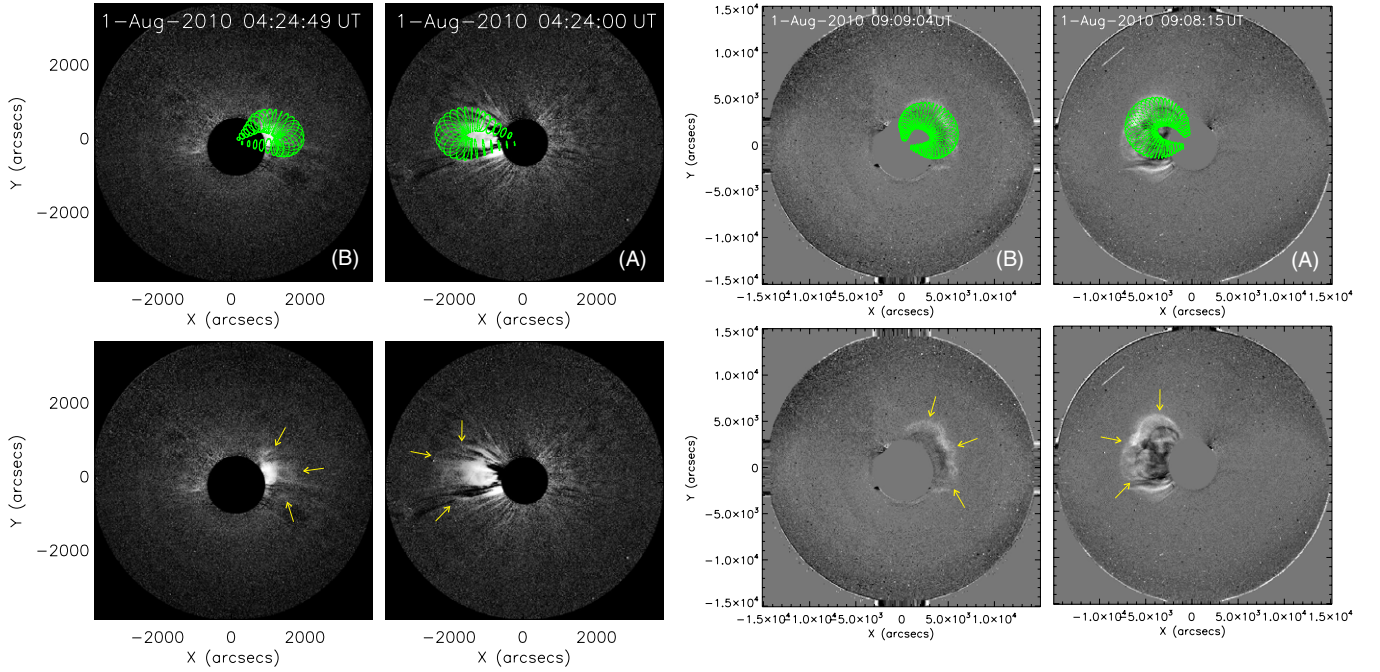
**Figure 4.** Results from forward modeling. Left: CME1 flux-rope simulation fitted to white-light data of COR1 on board *STEREO-A* (A) and *STEREO-B* (B). The radial back-projection of the CME apex onto the solar surface gives a location of E20/N09. Right: CME2 flux-rope simulation fitted to A and B white-light data of COR2, yielding a surface location of E28/N20. The identified boundary of each CME is marked with yellow arrows in the bottom panels.

(A color version of this figure is available in the online journal.)

E23° ± 15°. A large deviation from its associated SR (E35) is obtained for CME2 from the remote sensing and in situ (R+IS) method. This gives an average direction of E13 (E12 if we match the derivative of the converted elongation with the speed of the sheath region and E14 if we match the averaged arrival time of the sheath region at the *Wind* spacecraft). Inspecting the direction of motion for CME2 derived from other methods (forward modeling, polarimetric localization, HM) we obtain ∼E30–E35 which would be more consistent with the location of the SR.

Figure 6 shows speed and radial distance profiles for the leading edge of CME2 that have been derived from elongation measurements from COR1/COR2/HI1/HI2 ecliptic observations from *STEREO-A* using directions E13 and E30. The speed profile is derived by performing numerical differentiation of the distance–time data applying three-point Lagrangian interpolation. The error bars in the speed profile represent uncertainties in the measurements of the leading edge of CME2 and are calculated as the standard deviation of the derivative from errors in the distance–time data. As can be seen, starting at a distance of ∼20 $R_\odot$ a clear deviation especially in the distance profile is obtained, revealing that E30 would not fit the boundary conditions at 1 AU. For that reason we chose to use the direction E13 for conversion and to compare with the results from the drag model. We note that this might give hints toward some longitudinal deflection of CME2, which is also found by Liu et al. (2012). However, we cannot rule out artifacts in the direction finding due to the geometrical assumptions underlying the different methods.

Inspection of the speed profile of CME2 as given in the top panel of Figure 6 reveals that there were two distinctly different stages in the deceleration of CME2. The first one, characterized by a rapid deceleration of $a \approx -40$ m s$^{-2}$, lasted from ∼10 UT until ∼14 UT. After that deceleration decreased to $a \approx -2$ m s$^{-2}$. In Figure 7 we show the de-projected radial

distance profile of CME1 (results taken from the geometric triangulation method; see Liu et al. 2012) extrapolated using a polynomial fit of second order until the time of interaction with CME2. Although the exact time depends on the direction of motion used for converting elongation into radial distance the interaction takes place between approximately 13:30 UT and 15:30 UT. From this we are able to attribute the first deceleration stage to the interaction of CME2 with CME1, whereas in the second stage the deceleration is due solely to the interaction of the merged structure with the ambient solar wind. The kinematical profile shows that the rapid deceleration stage actually begins a few hours *before* the leading edges of CME1 and CME2 merged in the white-light data (∼10 UT), which can be attributed to a finite thickness of CME1.

From the results presented in Table 1, CME1 has a mean speed of ∼700 km s$^{-1}$ within the FoV of COR2 and a total ("true") mass of ∼6–8 × 10$^{15}$ g; in contrast CME2 is a much faster event with a mean speed of ∼1200 km s$^{-1}$ within the FoV of COR2 and has a total mass of ∼2–3 × 10$^{16}$ g.

Figure 8 shows the speed–distance, speed–time, and distance–time profiles of the leading edge of CME2 as derived from COR1/COR2/HI1/HI2 ecliptic observations from *STEREO-A*. The conversion to radial distance uses the result from the remote sensing and in situ method with E13 as ecliptic longitude. The speed profile and error bars are derived in the same way as given for Figure 6. The middle and bottom panels of Figure 8 show the speed–time and distance–time curves of CME2 overlaid with the results from the DBM simulating two different scenarios of CME evolution.

For calculating the kinematical profile of CME2 from the DBM we use $C_d = 1$ fixed over the Sun–Earth distance range, and constrain the other parameters by observations (see also Figure 9). The asymptotic solar wind speed $w$ at 1 AU before the arrival of CME2 was measured by *Wind* as ∼400 km s$^{-1}$ (see Harrison et al. 2012; Liu et al. 2012). There is no indication
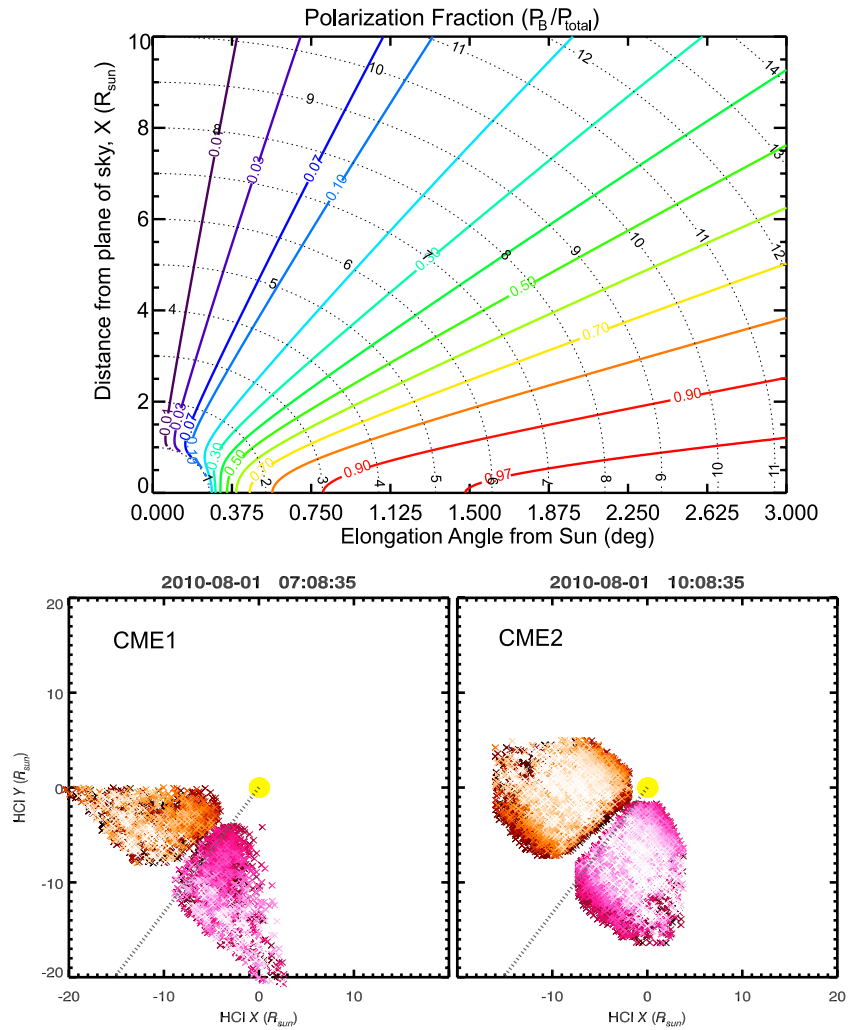
**Figure 5.** Top: visualization of Billings (1966) equations used to obtain a reconstructed point within a CME relative to the spacecraft plane-of-sky depending on the measured elongation and fractional polarization. Bottom: each plot shows two possible reconstructed CMEs for CME1 (left) and CME2 (right) based on *STEREO-A* percent polarization measurements. The correct reconstruction is eastward of the Sun–Earth line, colored reddish-orange. The Sun–Earth line is shown as dashed line extending from the Sun marked as yellow circle.

(A color version of this figure is available in the online journal.)

from in situ data that CME2 crossed a high-speed solar wind stream during its propagation from Sun to Earth, which would result in a strong variation of the background solar wind speed $w$ (see also Temmer et al. 2011). From the observational results of CME2 we derive $t_0$ to be 2010 August 1 10:19 UT and $v_0 = 1400$ km s$^{-1}$ at $R_0 = 15\ R_\odot$. We first calculate the kinematical profile DBM1 assuming that CME2 moves in unperturbed solar wind conditions from Sun to Earth. The parameter $\gamma$ is kept constant over the Sun–Earth distance range and chosen to be $\gamma = 0.25 \times 10^{-7}$ km$^{-1}$, representing a CME which moves in an unperturbed environment of lower density and lower speed than the CME itself (see also the parameter study by Cargill 2004). As can be seen, the results from DBM1 based on such an assumption do not match the observational results. In another approach we calculate DBM2 using the same values for $t_0$, $v_0$, and $R_0$ but changing $w$ and $\gamma$ at a distance of $35\ R_\odot$, which is the distance at which the interaction of the two CMEs is likely to be finished. With this we simulate a scenario in which a CME moves up to $35\ R_\odot$ in an ambient flow that is of higher speed and density than the unperturbed environment. Beyond $35\ R_\odot$, CME1 and CME2 move as single structure in an ambient flow of speed and density comparable to an unperturbed solar wind,

having the cross section of CME2 and the combined mass of CME1 and CME2. In order to match the observational results, for radial distances $\leqslant 35\ R_\odot$ we used $\gamma_1 = 1.65 \times 10^{-7}$ km$^{-1}$ and $w_1 = 600$ km s$^{-1}$, and for radial distances $> 35\ R_\odot$ we used $\gamma_2 = 0.2 \times 10^{-7}$ km$^{-1}$ and $w_2 = 400$ km s$^{-1}$ (cf. Figure 9).

In order to reproduce the CME–CME interaction in DBM2 we used values that give $\gamma_1/\gamma_2 = 8.25$. According to the CME–CME interaction scenario as described above we may express $\gamma_1 = (A_{\mathrm{CME2}}\rho_{\mathrm{CME1}})/(m_{\mathrm{CME2}})$ and $\gamma_2 = (A_{\mathrm{CME2}}\rho_{\mathrm{sw}})/(m_{\mathrm{CME1}} + m_{\mathrm{CME2}})$ from which we obtain

$$\frac{\gamma_1}{\gamma_2} = \frac{\rho_{\mathrm{CME1}}(m_{\mathrm{CME1}} + m_{\mathrm{CME2}})}{\rho_{\mathrm{sw}} m_{\mathrm{CME2}}}.$$

We now compare $\rho_{\mathrm{CME1}}$ and $\rho_{\mathrm{sw}}$ at a distance of $35\ R_\odot$. Assuming a cone model (e.g., Michalek 2006), we calculate the volume of CME1 using the derived width of $\sim68°$. Using the total mass of CME1 of $\sim6$–$8 \times 10^{15}$ g implies $\rho_{\mathrm{CME1}} \sim 1.0 \times 10^{-21}$ g cm$^{-3}$. Applying the model by Leblanc et al. (1998) for the solar wind density we obtain $\rho_{\mathrm{sw}} \sim 4.5 \times 10^{-22}$ g cm$^{-3}$ (cf. Vršnak et al. 2010). This gives us $\rho_{\mathrm{CME1}} \approx 2\ \rho_{\mathrm{sw}}$. From total mass calculations we obtain $m_{\mathrm{CME2}} \approx 3\ m_{\mathrm{CME1}}$. Beyond $\sim10\ R_\odot$ the mass is assumed to remain constant (Colaninno & Vourlidas
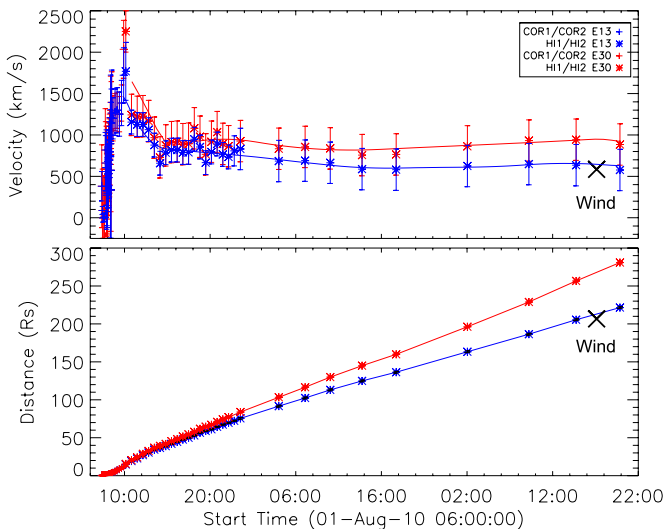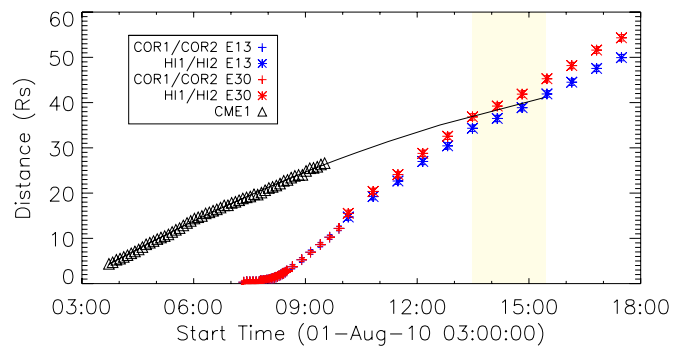
**Figure 6.** Top: velocity–time plot of CME2 using different directions for converting measured elongations into radial speed. Measured in situ speed of the sheath region from *Wind* is indicated with "×". Bottom: distance–time plot of CME2 using different directions for converting measured elongations into radial distance. Measured arrival time of the shock at the *Wind* spacecraft is indicated with "×". The error bars are the standard deviation from the derivatives and represent the uncertainties in the measurements.

(A color version of this figure is available in the online journal.)

2009) from which we suppose that the ratio between the masses is constant. We note that this is a simplistic assumption since Lugaz et al. (2005) have shown from simulations that the mass of a CME might increase up to a distance of 1 AU. From this we derive $\gamma_1/\gamma_2 \sim 3$, which shows that there is discrepancy to the model results. We may speculate that, besides the aerodynamic drag effect, magnetic forces (i.e., magnetic tension and magnetic pressure gradients raised due to the interaction) significantly contributed to the enhanced deceleration of CME2.

## 5. DISCUSSION AND CONCLUSION

Applying currently available models and reconstruction techniques for observations of the CME events from 2010 August 1 we are able to analyze a CME–CME interaction process quantitatively. Keeping in mind that the three-dimensional reconstruction techniques are only approximate and the kinematic results may vary greatly (see, e.g., Lugaz et al. 2010), we use several (independent) methods. The results derived for the three-dimensional propagation directions are in agreement and provide evidence that a full interaction takes place between two consecutively launched CMEs. From observations we derive that the faster CME (CME2) is about three times more massive and ~30% larger in volume than the slower preceding CME (CME1). The white-light signatures of the CMEs obtained from heliospheric imagery show that CME1 seems to be "lost" within the structure of CME2 since there are no features that can be attributed to CME1 after interaction (see also Harrison et al. 2012). What we observe in white light as the leading edge of CME2 after merging with CME1 most probably includes the mass of CME1. Whether the magnetic features really merge, i.e., reconnect, or whether CME1 stays as a magnetic entity that is compressed and pushed forward by CME2, is not possible to derive from remote sensing data. In situ data give more information on this aspect and are discussed in detail by Liu et al. (2012). The results by these authors show that the multi-point



**Figure 7.** Velocity–time plot of CME2 using different directions for converting measured elongations into speed together with the kinematical profile of CME1 (geometric triangulation method) and its interaction time with CME2 (marked with a shaded box) using a polynomial fit of second order for extrapolation.

(A color version of this figure is available in the online journal.)

in situ observations are consistent with compression of CME1 rather than its disintegration.

The CME–CME interaction is associated with transfer of momentum between the ejecta (Farrugia & Berdichevsky 2004) and this might be compared to simplified scenarios of one-dimensional elastic and inelastic collision (cf. Lugaz et al. 2009). At the time of interaction at about 10 UT, the speed of CME1 is ~600 km s$^{-1}$ and CME2 ~1400 km s$^{-1}$, and the total mass of CME2 is derived to be ~3 times higher than for CME1. Assuming a full interaction in the form of a perfectly inelastic collision, we would expect CME2 to move with a speed of ~1200 km s$^{-1}$. Assuming an elastic collision, CME1 would experience an acceleration, reaching a speed of ~1800 km s$^{-1}$. From observations, we derive a speed for the leading edge of the merged structure at about 15 UT of ~800 km s$^{-1}$ that makes both scenarios unlikely. As derived from the polarimetric localization method and the forward modeling (cf. Figures 4 and 5), CME2 is significantly larger than CME1, from which it is not hard to imagine that CME1 will be "lost" within CME2. However, given the differences in size as well as mass, it is hard to imagine how the interaction between the two CMEs could result in substantial deceleration of CME2. Nevertheless, we must not forget that we are dealing with magnetic structures. As reported for the early kinematical evolution of CMEs, the interaction with strong overlying coronal magnetic fields may cause enhanced deceleration (e.g., Temmer et al. 2008, 2010).

By applying the DBM proposed by Vršnak & Žic (2007) and advanced by Vršnak et al. (2012), we are able to simulate the kinematical profile of CME2. The observational results can be reproduced by varying $\gamma$ values and ambient flow speeds in the drag formula at a radial distance from the Sun of ~35 $R_\odot$ (the distance at which the interaction process is likely to be finished). This can be interpreted in such a way that CME1 represents an MHD obstacle for CME2, which leads to increased deceleration. In other words, CME2 propagates into a medium of denser plasma, higher flow speed, and stronger magnetic field than the unperturbed solar wind. After the interaction process the merged entity, i.e., CME2, carries the sum of masses of CME1 and CME2 and moves on as a single structure through an ambient flow of speed and density typical for quiet solar wind conditions.

Inspecting the kinematical profile of CME2 we derive that the strong deceleration starts a few hours before the merging of the white-light leading edge signatures of the CMEs (10 UT versus ~14 UT). This can be interpreted as an interaction between
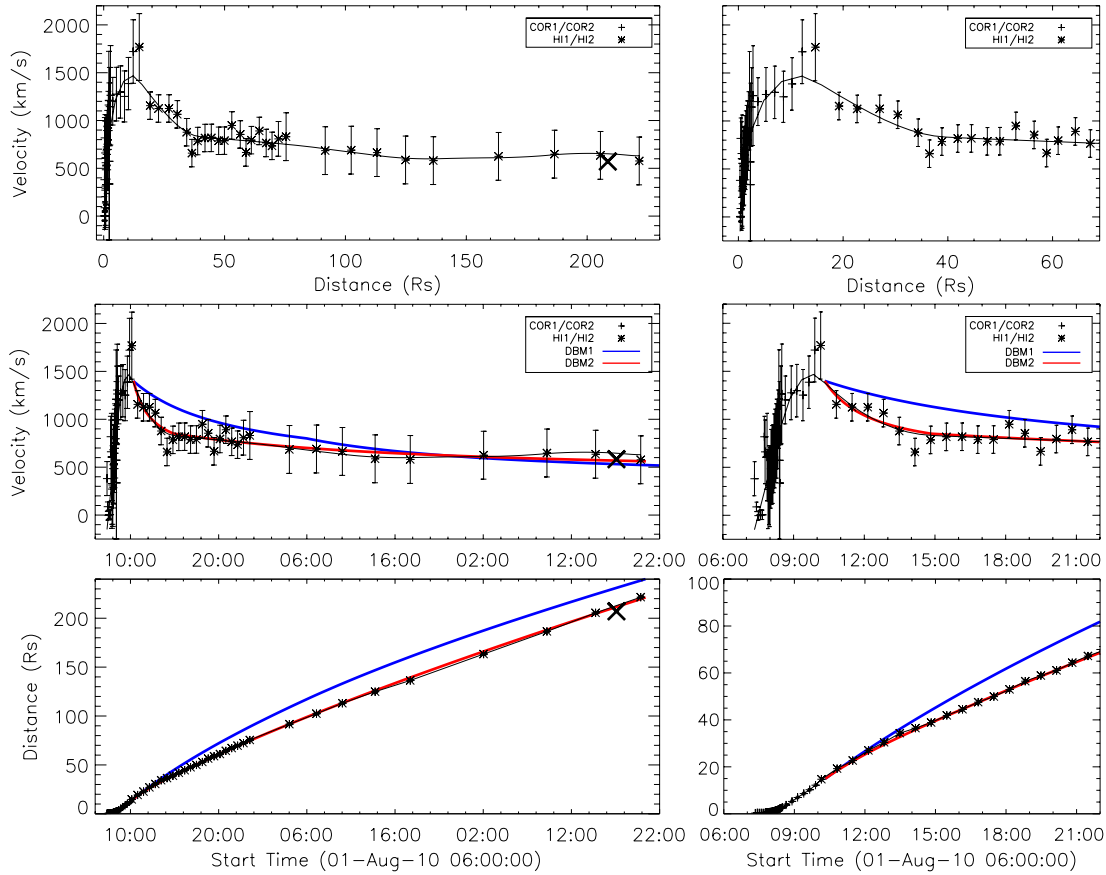
**Figure 8.** Top: velocity–distance plot of CME2. Middle: velocity–time plot of CME2 overlaid with the results from DBM1 (blue solid line; non-varying $\gamma$) and DBM2 (red solid line; varying $\gamma$ simulating the CME–CME interaction; see also Figure 9). Bottom: distance–time plot of CME2 overlaid with the results from DBM1 and DBM2. The black solid line is the spline fit to the observational data. The right-hand panels are expanded portions of the left-hand panels showing in detail the deceleration phase of CME2. Measured in situ parameters from *Wind* are indicated with "×" in the left-hand panels. The error bars are the standard deviation from the derivatives and represent the uncertainties in the measurements.

(A color version of this figure is available in the online journal.)
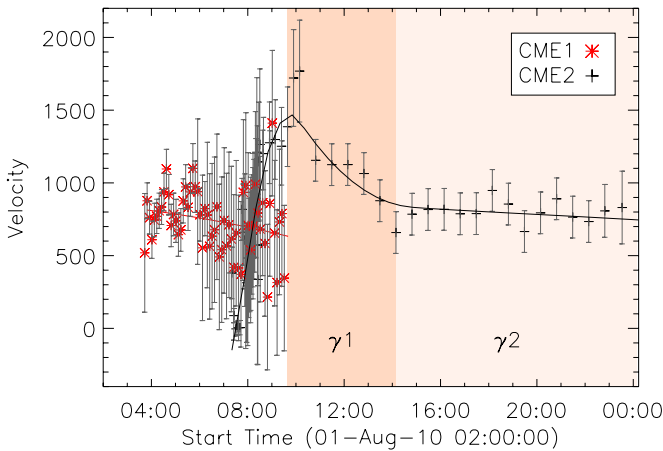


**Figure 9.** Velocity–time profile of CME1 (geometric triangulation method) and CME2. The shaded areas mark the range during which varying $\gamma$ values are applied. The error bars are the standard deviation from the derivatives and represent the uncertainties in the measurements. The red solid line represents a polynomial fit of second order to velocity data for CME1. The black solid line is the spline fit to the velocity data for CME2.

(A color version of this figure is available in the online journal.)

their magnetic structures, i.e., by a finite thickness of CME1. As shown at the end of Section 4, observations favor a scenario in which magnetic forces, induced during the CME–CME interaction, may play a substantial role in decelerating CME2.

We speculate that the increase in magnetic tension and pressure when CME2 bends and compresses the magnetic field lines of CME1 increases the efficiency of drag. We would like to note that the interaction lasted for about ∼4–5 hr, which is probably too short for the total reconnection of the magnetic flux in CME1. This might support the results by Liu et al. (2012) who suggest that CME1 and CME2 most probably remain as two independent magnetic structures.

A metric type II burst emitted from two radio sources moving with different speeds is recorded at 09:50–10:15 UT, which is indicative of an interaction process (Gopalswamy et al. 2001, 2002). This supports the conclusion that the start of the interaction process is represented in the kinematical profile of CME2 by the strong deceleration observed around 10 UT. A detailed study for the 2010 August 1 events with respect to radio observations is given by Martinez Oliveros et al. (2012).

CME–CME interaction processes are still not well understood, mostly due to the lack of appropriate observational data to give information on the three-dimensional characteristics of CMEs. Interaction processes between ejecta are also important with respect to forecasting the arrival times of Earth-directed CME events and their enhanced geoeffectiveness (e.g., Burlaga et al. 1987). As has been shown in the present study, the kinematic profile of a CME can be significantly changed due to the interaction with a preceding slower CME. Especially in times of enhanced solar activity, CMEs cannot be treated as isolated events. Analytical models in combination with unprecedented

observations and three-dimensional reconstruction techniques are powerful tools which give us deeper insight and help us to better understand the evolution of CME events in IP space.

## REFERENCES

Batchelor, G. K. 1967, Phys. Fluids, 10, 302
Billings, D. E. (ed.) 1966, A Guide to the Solar Corona (New York: Academic)
Burlaga, L. F., Behannon, K. W., & Klein, L. W. 1987, J. Geophys. Res., 92, 5725
Burlaga, L. F., Plunkett, S. P., & St. Cyr, O. C. 2002, J. Geophys. Res. (Space Phys.), 107, 1266
Cargill, P. J. 2004, Sol. Phys., 221, 135
Cargill, P. J., Chen, J., Spicer, D. S., & Zalesak, S. T. 1996, J. Geophys. Res., 101, 4855
Chen, J. 1996, J. Geophys. Res., 101, 27499
Colaninno, R. C., & Vourlidas, A. 2009, ApJ, 698, 852
Cremades, H., & Bothmer, V. 2004, A&A, 422, 307
Davies, J. A., Harrison, R. A., Rouillard, A. P., et al. 2009, Geophys. Res. Lett., 36, L02102
de Koning, C. A., & Pizzo, V. J. 2011, Space Weather, 90, S03001
Farrugia, C., & Berdichevsky, D. 2004, Ann. Geophys., 22, 3679
Gopalswamy, N., Thompson, W. T., Davila, J. M., et al. 2009, Sol. Phys., 259, 227
Gopalswamy, N., Yashiro, S., Kaiser, M. L., Howard, R. A., & Bougeret, J.-L. 2001, ApJ, 548, L91
Gopalswamy, N., Yashiro, S., Michałek, G., et al. 2002, ApJ, 572, L103
Harrison, R. A., Davies, J. A., Möstl, C., et al. 2012, ApJ, in press
Howard, R. A., Moses, J. D., Vourlidas, A., et al. 2008, Space Sci. Rev., 136, 67
Howard, T. A., & Tappin, S. J. 2009, Space Sci. Rev., 147, 31
Jacques, S. A. 1977, ApJ, 215, 942
Kahler, S. 1994, ApJ, 428, 837
Kahler, S. W. 2001, J. Geophys. Res., 106, 20947
Kahler, S. W., & Webb, D. F. 2007, J. Geophys. Res. (Space Phys.), 112, 9103
Leblanc, Y., Dulk, G. A., & Bougeret, J.-L. 1998, Sol. Phys., 183, 165
Lepping, R. P., Acũna, M. H., Burlaga, L. F., et al. 1995, Space Sci. Rev., 71, 207
Liu, R., Liu, C., Wang, S., Deng, N., & Wang, H. 2010a, ApJ, 725, L84
Liu, Y., Davies, J. A., Luhmann, J. G., et al. 2010b, ApJ, 710, L82
Liu, Y., Luhmann, J. G., Bale, S. D., & Lin, R. P. 2009, ApJ, 691, L151
Liu, Y., Thernisien, A., Luhmann, J. G., et al. 2010c, ApJ, 722, 1762
Liu, Y. D., Luhmann, J. G., Möstl, C., et al. 2012, ApJ, 746, L15
Low, B. C. 2001, J. Geophys. Res., 106, 25141
Lugaz, N. 2010, Sol. Phys., 267, 411
Lugaz, N., Hernandez-Charpak, J. N., Roussev, I. I., et al. 2010, ApJ, 715, 493
Lugaz, N., Manchester, W. B., IV, & Gombosi, T. I. 2005, ApJ, 634, 651
Lugaz, N., Vourlidas, A., & Roussev, I. I. 2009, Ann. Geophys., 27, 3479
Lugaz, N., Vourlidas, A., Roussev, I. I., et al. 2008, ApJ, 684, L111
Martinez Oliveros, J. C., Raftery, C. L., Bain, H. M., et al. 2012, ApJ, 748, 66
Michalek, G. 2006, Sol. Phys., 237, 101
Mierla, M., Inhester, B., Antunes, A., et al. 2010, Ann. Geophys., 28, 203
Möstl, C., Farrugia, C. J., Temmer, M., et al. 2009, ApJ, 705, L180
Möstl, C., Temmer, M., Rollett, T., et al. 2010, Geophys. Res. Lett., 37, L24103
Möstl, C., et al. 2012, ApJ, in press
Ogilvie, K. W., Chornay, D. J., Fritzenreiter, R. J., et al. 1995, Space Sci. Rev., 71, 55
Ontiveros, V., & Vourlidas, A. 2009, ApJ, 693, 267
Rollett, T., Möstl, C., Temmer, M., et al. 2012, Sol. Phys., 276, 293
Rouillard, A. P., Davies, J. A., Forsyth, R. J., et al. 2008, Geophys. Res. Lett., 35, L10110
Schmidt, J., & Cargill, P. 2004, Ann. Geophys., 22, 2245
Schrijver, C. J., & Title, A. M. 2011, J. Geophys. Res. (Space Phys.), 116, A04108
Sheeley, N. R., Walters, J. H., Wang, Y.-M., & Howard, R. A. 1999, J. Geophys. Res., 104, 24739
Sheeley, N. R., Jr., Herbst, A. D., Palatchi, C. A., et al. 2008, ApJ, 675, 853
Temmer, M., Rollett, T., Möstl, C., et al. 2011, ApJ, 743, 101
Temmer, M., Veronig, A. M., Kontar, E. P., Krucker, S., & Vršnak, B. 2010, ApJ, 712, 1410
Temmer, M., Veronig, A. M., Vršnak, B., et al. 2008, ApJ, 673, L95
Thernisien, A. 2011, ApJS, 194, 33
Thernisien, A., Vourlidas, A., & Howard, R. A. 2009, Sol. Phys., 256, 111
Thernisien, A. F. R., Howard, R. A., & Vourlidas, A. 2006, ApJ, 652, 763
Vršnak, B. 2001, Sol. Phys., 202, 173
Vršnak, B., & Gopalswamy, N. 2002, J. Geophys. Res. (Space Phys.), 107, 1019
Vršnak, B., & Žic, T. 2007, A&A, 472, 937
Vršnak, B., Žic, T., Falkenberg, T. V., et al. 2010, A&A, 512, A43
Vršnak, B., et al. 2012, Sol. Phys, submitted
Webb, D. F., Howard, T. A., Fry, C. D., et al. 2009, Sol. Phys., 256, 239
Wuelser, J., Lemen, J. R., Tarbell, T. D., et al. 2004, Proc. SPIE, 5171, 111